Topological states of Sr_3PbO: From topological crystalline insulator phase in the bulk to quantum spin Hall insulator phase in the thin-film limit

Hei Lam, Rui Peng, Ziyu Wang, Chunyu Wan, and Junwei Liu*
Department of Physics, Hong Kong University of Science and Technology, Kowloon, Hong Kong 518000, China

(Received 15 July 2023; revised 1 October 2023; accepted 5 October 2023; published 24 October 2023)

Nontrivial topological materials are emerging as fascinating objects in condensed matter research due to their great potential in low-power and low-dissipation electronic applications. In this work, using first-principles calculations and a tight-binding method, we propose a promising candidate with novel topological states and high experimental feasibility. We prove that Sr_3PbO exhibits a topological crystalline insulator (TCI) phase in its three-dimensional (3D) bulk lattice and a quantum spin Hall insulator (QSHI) phase in its two-dimensional (2D) thin film, presenting a picture of evolution from 3D TCI to 2D QSHI. Moreover, the topological phase transition between QSHI and trivial phases occurs as the thickness of the thin-film Sr_3PbO varies. This intriguing behavior can also be confirmed using a low-energy effective model with infinite potential well boundary conditions. The high-quality bulk and thin-film Sr_3PbO have been prepared in an experiment, implying high feasibility for experimental characterization.

DOI: 10.1103/PhysRevB.108.155139

I. INTRODUCTION

Recent years have witnessed an outburst of research activities on topological phases such as topological insulators (TIs) [1–4], topological crystalline insulators (TCIs) [5–9], and topological semimetals [10–13]. They are characterized by the gapless surface/edge states inside the bulk gap, which are robust against elastic backscattering and localization. Therefore, topological materials hold great potential in quantum electronic devices with low heat dissipation and power consumption. In addition to individual topological phases, topological phase transition between different topological phases has also attracted enormous interest. For example, the transition between type-I and type-II Weyl fermions can be observed in ternary transition metal chalcogenides by tuning van der Waals interlayer spacing [14]; the topological phase in $MnBi_2Te_4$ exhibits an oscillatory behavior as the thickness changes [15].

Sr_3PbO has been known since 1980 [16]. It harbors a variety of new physics such as superconductivity [17,18], giant magnetoresistance [19,20], and superionic conductivity [21,22]. In particular, it was identified as a candidate TCI with surface states protected by mirror symmetry [23], though a full analysis of its surface states is still lacking. Encouragingly, a high-quality thin-film Sr_3PbO along the [001] direction was prepared by the molecular beam epitaxy (MBE) method [24]. It is natural to ask whether or not the thin-film system can exhibit novel topological states. However, up to now, the topological properties of the thin film have not been explored. Therefore, it is highly desirable to provide a comprehensive study on bulk and thin-film Sr_3PbO.

In this work, we report a detailed study on the nontrivial topological states of bulk and thin-film Sr_3PbO. In Sec. II, we provide the details of our first-principles calculations. In Sec. III, we give a full analysis of the surface states in (001), (110), and (111) lattice planes in bulk Sr_3PbO. In Sec. IV, we prove that the thin films with Sr_2-O terminations are the stablest ones among three different configurations. Due to the limitation of the computational cost in the first-principles calculations, we build a thin-film model from the bulk tight-binding Hamiltonian in Sec. V. Remarkably, we demonstrate the existence of a quantum spin Hall insulator (QSHI) phase and unveil the topological phase transitions between QSHI and trivial states in thin films. Based on the previously proposed method for the crossover state between three-dimensional (3D) TI and two-dimensional (2D) QSHI [25], we show the connection between 3D TCI and 2D QSHI in our model.

II. METHODS

First-principles calculations were performed using the Vienna *ab initio* simulation package (VASP) [26] based on density functional theory with the projector augmented-wave method [27]. We chose the experimental value $a = 5.15$ Å for the lattice constant of the bulk Sr_3PbO [24]. The Heyd-Scuseria-Ernzerhof (HSE06) functional with mixing parameter $a = 0.25$ and adjustable parameter $w = 0.2$ was used to give a more accurate band gap result [28]. The cutoff energy of the plane wave basis was set to 560 eV, and the $7\times7\times7$ k-point meshing was used to sample the Brillouin zone. For the band structure calculations of the thin films, the Perdew-Burke-Ernzerhof generalized gradient approximation [29] with a $9\times9\times1$ k-point mesh was used. To fit the tight-binding model, the Wannier90 software package was used to generate the tight-binding matrix with the maximally

*liuj@ust.hk

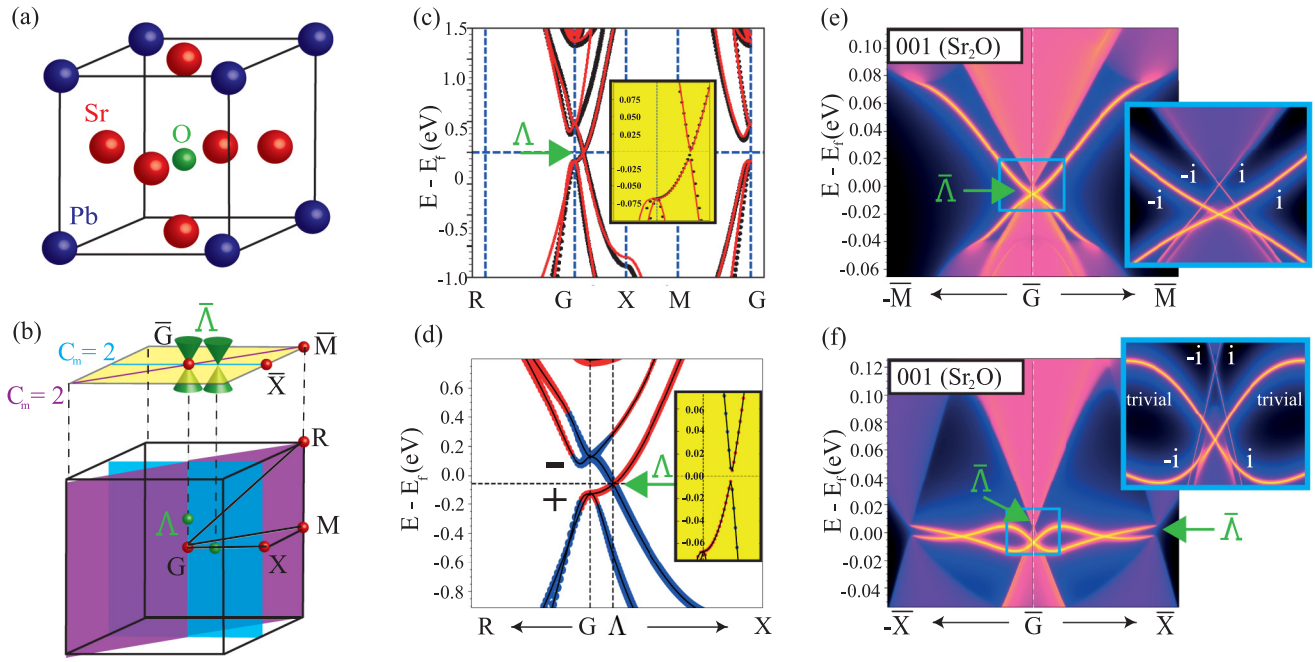

FIG. 1. (a) The lattice structure of bulk Sr_3PbO. (b) The bulk Brillouin zone and the projective Brillouin zone along [001] direction. (c) The band structures of bulk Sr_3PbO from first-principles calculations (black dots) and fitted tight-binding model (red solid lines). (d) The projected orbitals with inverted band ordering near Λ point (red dots correspond to $Sr-d$ orbitals, and blue dots correspond to $Pb-p$ orbitals). [(e), (f)] Surface density of states in (001) with Sr_2-O termination, and $\pm i$ in the insets indicate the mirror eigenvalues.

localized Wannier function (MLWF) [30]. A 3×3×3 k-point mesh was chosen in the fitting. After doing the projection analysis, we found that the band structure around the Fermi level is mainly contributed by $Sr-d$ orbitals and $Pb-p$ orbitals. Three $Pb-p$ orbitals and five $Sr-d$ orbitals were chosen as bases to make sure the avoided crossing can be obtained near the $\bar{G}$ point [31]. Including the spin degrees of freedom, we had in total $3\times2+(5\times3\times2)=36$ bases in our tight-binding Hamiltonian.

III. SURFACE STATE ANALYSIS OF SR_3PbO

As shown in Figs. 1(a) and 1(b), the bulk Sr_3PbO is in the space group $Pm\bar{3}m$ with a simple-cubic Brillouin zone. The band structures obtained from the first-principles calculations are shown in Figs. 1(c) and 1(d). We can see that the fundamental gap of bulk Sr_3PbO is located at the Λ point in the G-X line. The $Pb-p$ orbitals on the valence band maxima (VBM) and $Sr-d$ orbitals on the conduction band minima (CBM) are inverted at the Λ point, which indicates the nontrivial topological nature. To show the nontrivial topological properties explicitly, we directly calculated the surface states on (001), (110), and (111) surfaces from the first-principles tight-binding models using the recursive Green's function method [32].

The results of the (001) surface with Sr_2-O termination are shown in Figs. 1(e) and 1(f), and other results can be found in Appendix A. From Figs. 1(e) and 1(f), we can see several Dirac cones with a small gap (indicated by the green arrow) along different high-symmetry lines around the $\bar{G}$ point. Due to the high symmetry of bulk Sr_3PbO, there are in total six equivalent gapped Dirac cones along three different rotational axes in the Brillouin zone. From the projective Brillouin zone along the [001] direction and the bulk Brillouin zone in Fig. 1(b), we can see that two Dirac cones at the Λ points along k_z will be projected to the $\bar{G}$ point, and another four equivalent gapped Dirac cones along four equivalent $\bar{G}$-$\bar{X}$ directions connected by the C_4 symmetry will be projected to four equivalent $\bar{\Lambda}$ points.

As shown in Fig. 1(b), there are two mirror reflection lines along $\bar{G}$-$\bar{X}$ and $\bar{G}$-$\bar{M}$ directions on the projective Brillouin zone. They come from the mirror reflection planes (100) and (110) on the bulk Brillouin zone, respectively. According to our previous work, (100) and (110) are both mirror reflection invariant planes with nonzero mirror Chern number $C_m=2$ [23]. To confirm this, we constructed the symmetry operators, transformed the tight-binding Hamiltonian into a block-diagonalized form with $\pm i$ subspace, and calculated C_m of each subspace independently [33]. The detailed calculation method and the explicit representation of the symmetry operators are included in Appendix B. The nonzero $C_m=2$ indicates that there must be two pairs of surface states with opposite mirror eigenvalues on the boundary of (100) and (110). As shown in Fig. 1(e), two gapless crossings induced by two pairs of states from the $\pm i$ subspaces can be observed in the small gapped region and the valence bulk region at $\bar{G}$ point, respectively. From Fig. 1(f), we can see one pair of nontrivial surface states crossing in the small gapped region at the $\bar{G}$ point, and the other pair of nontrivial surface states connecting the valence region to the conduction region along the $\bar{G}$-$\bar{X}$ direction. There is an additional trivial surface state along the $\bar{G}$-$\bar{X}$ direction, which does not connect the valence region to the conduction region. As a result, a crossing induced by the trivial and nontrivial states can be observed near the $\bar{G}$ point.

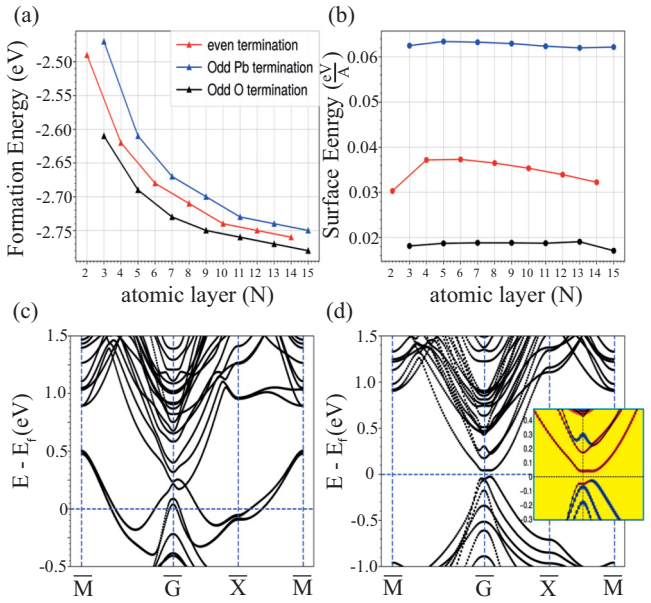

FIG. 2. (a) Formation energy of three different thin-film configurations as a function of atomic layers. (b) The surface energy of three different thin-film configurations as a function of atomic layers. The unit of A denoted as the total area of the thin film, which is in the unit of $Å^2$. (c) Band structure of 9-layer thin film with Sr_2-O terminations. (d) Band structure of 9-layer Cl-passivated thin film. The inset shows the inverted band ordering nature (red dots represent the $Sr - d_{z^2}$ orbitals, and blue dots represent the $Pb - p_y$ orbitals).

IV. STABILITY OF THE THIN FILM FROM DFT

In view of the rich topological properties of the bulk system, we also analyzed the thin-film system to explore its edge states. With the nontrivial topological surface states confirmed, we can expect to realize 2D topological phases due to the hybridization between top and bottom surface states in the thin films of Sr_3PbO as in the thin films of Bi_2Se_3-type 3D TIs [25] and SnTe-type TCIs [34]. To give a reliable experimental prediction, we first study the stability of different thin films. The thin films along the [001] direction have two types of terminations (Sr-Pb termination and Sr_2-O termination). Therefore, there will be three configurations: an even-atomic-layer-thick configuration with two types of terminations and two odd-atomic-layer-thick configurations with either Sr-Pb or Sr_2-O terminations. To find out the stablest configuration, we calculated the formation energy and surface energy of the thin-film systems. The formation energy is calculated using the formula $E_{fm} = \frac{E_s - \sum_x n_x \mu_x}{\sum_x n_x}$, where E_s denotes the total energy of the slab, n_x denotes the number of x atoms in the unit cell of the thin film, and μ_x denotes the chemical potential of the element obtained in their corresponding stable bulk phases (for example, the chemical potential of oxygen is the energy of the oxygen molecule divided by 2) [35]. As we can see in Fig. 2(a), the formation energies of these three configurations all exhibit a decreasing tendency as we increase the number of atomic layers up to 15. We expect the formation energy will continue to decrease, which implies the stability of bulk Sr_3PbO. Among the three configurations, the thin films with Sr_2-O termination have the lowest formation energy.

The surface energy is defined as $\sigma = \frac{E_s - nE_b}{2A}$, where n is the total number of atoms in the thin film, and E_b is the bulk energy of each atom [36]. The linear fitting and Boettger method [37,38] are both used to approximate the E_b. As shown in Figs. 2(a) and 2(b), the thin films with Sr_2-O termination have the lowest surface energy among the three configurations. The results of formation energy and surface energy indicate that the thin film with Sr_2-O termination is the stablest configuration.

Based on the results above, we calculated the band structure of a 9-layer thin film with Sr_2-O termination and plotted it in Fig. 2(c). Each energy band is twofold degenerate due to time-reversal symmetry and inversion symmetry. However, the fundamental gap of the thin-film system has a negative value, exhibiting a metallic nature. This can be attributed to the dangling bond effect of extra charge induced by the unpaired electron on the surface. To eliminate the dangling bond effect, the Cl atom was chosen for passivation. The band structure of Cl-passivated thin film is shown in Fig. 2(d). As we can see, the insulating property is successfully recovered after the passivation. Moreover, the inverted ordering of orbitals still holds in the band structure, as shown in the inset of Fig. 2(d).

V. TOPOLOGICAL PHASE TRANSITION OF THIN-FILM SYSTEM

We next investigated the topological properties of Sr_3PbO thin films with different thicknesses. Due to the high computational cost, we will mainly use the tight-binding models with parameters extracted from the first-principles calculations. The band gap at the G point, the fundamental gap, and the minimum direct gap as a function of thickness are shown in Fig. 3(a). Interestingly, three types of band gaps show oscillation behaviors as the thickness increases, which indicates multiple topological phase transitions at specific critical thicknesses.

To explicitly study the topological phase transition, we calculated the edge states of thin films with different thicknesses. Remarkably, all the thin films thinner than 9 layers are confirmed to be a trivial insulator without helical edge states, and the thin films with thickness from 11 layers and 19 layers are nontrivial with a pair of helical edge states as shown in Figs. 3(c) and 3(d). Different from the TCI phase in bulk Sr_3PbO, the helical edge states in 11-layer thin film correspond to the QSHI phase with the Kramers pair at the time-reversal-invariant momentum point (TRIM). The edge states of the thin films with larger thicknesses around the critical thickness are shown in Appendix C. We can see that the system becomes topologically trivial again at 23 atomic layers and turns to the QSHI phase at 35 atomic layers.

Considering the thickness of thin film decreases to a value that is comparable to the spread of the wave functions on top and bottom surfaces, the hybridization of the wave functions opens up a large gap at the $\bar{G}$ point. Since the odd-atomic-layer thin films have the same surface terminations on both surfaces, they can be described with a single valley Dirac-like

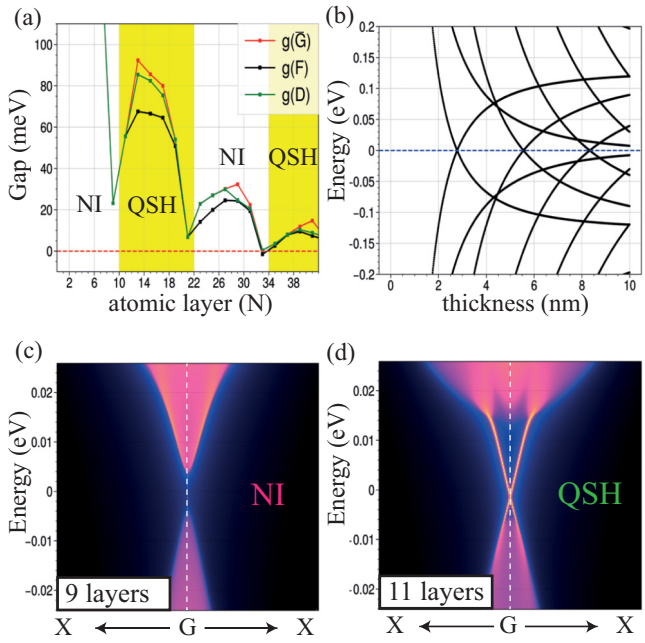

FIG. 3. (a) Band gap at G point $g(\bar{\Gamma})$, the fundamental gap $g(F)$, and the minimum of the direct gap in the entire Brillouin zone $g(D)$ as a function of the atomic layers. (b) Phase diagram of thin-film Sr_3PbO with varying thicknesses. (c) The edge states of the 9-layer system. (d) The edge states of the 11-layer system.

Hamiltonian with a mass term representing the coupling between the top and bottom surfaces [39].

The topological phase transition in the thin film can be understood as the crossover between 3D TI and 2D QSHI as in Bi_2Se_3 [25]. For bulk Sr_3PbO, the general low-energy effective $k \cdot p$ Hamiltonian at the G point [23] that satisfies all the cubic point group symmetries is

$$H(k) = (m + \alpha k^2)\tau_z + v_1 \tau_x k \cdot J + v_2 \tau_x k \cdot \widetilde{J}, \qquad (1)$$

where spin 3/2 is taken as basis, and the matrices J and $\widetilde{J}$ correspond to spin 3/2 matrices and a set of matrices that transform under the cubic point group symmetry. These matrix representations are provided in the Supplemental Materials of [23]. The $k \cdot p$ model preserves the entire cubic point group symmetry and can accurately represent the energy dispersion around the Gamma point. To establish the connection between 3D TCI and 2D QSHI, we can model the system as a quantum well structure by setting up an infinite potential barrier at top and bottom surfaces. The problem can be greatly simplified because the Dirac cone only occurs around $\bar{G}$. If we use the boundary condition where $\psi(z)$ vanishes at the $z = 0$ and $z = d$ regions and considering the vicinity of $\bar{G}$ point, we have the following simplified 2D $k \cdot p$ Hamiltonian:

$$H(\bar{G}) = \begin{pmatrix} m - \alpha \frac{d^2}{dz^2} & (v_1 J_z + v_2 \widetilde{J}_z) i \frac{d}{dz} \\ (v_1 J_z + v_2 \widetilde{J}_z) i \frac{d}{dz} & -m - \alpha \frac{d^2}{dz^2} \end{pmatrix}. \qquad (2)$$

The problem becomes solving the eigenvalues of a set of coupled differential equations. We can numerically solve the energy spectrum by discretizing the Hamiltonian with the finite difference method. Due to the quantum confinement effect, the valence band and the conduction band are quantized into discrete electron and hole energy subbands for a given thickness. As shown in Fig. 3(b), there are some crossings for the electron subband and hole subband at specific values of d. By calculating the interval between d_{i+1} and d_i, we found that they have a roughly equal spacing of around 2.8 nm, which is close to the result obtained from the tight-binding method (around 2.575 nm). We further calculated the parity of the electron and hole subbands closest to $E = 0$, and found that the parity of the electron subband and hole subband are flipped after it passes through each gap closing point, which confirms the topological phase transition with the thickness.

VI. CONCLUSIONS

To summarize, we showed that bulk and thin-film Sr_3PbO contain nontrivial topological properties. We did a deep analysis to show the nontrivial surface states protected by the crystal point group symmetry in bulk Sr_3PbO. The calculated surface states can be used for further experimental verification in the ARPES experiment. For thin-film Sr_3PbO, the odd-atomic-layer thin film with Sr_2-O termination is the stablest among three different thin-film configurations. Remarkably, the topological phase transition between the QSHI and trivial phases is identified in thin-film Sr_3PbO, which is confirmed by both realistic tight-binding models and low-energy effective theory. Moreover, our results and conclusion can be generated for other antiperovskite TCIs and can be used as guidance for further experimental verification.

ACKNOWLEDGMENT

This work is supported by the National Key R&D Program of China (Grant No. 2021YFA1401500), the Hong Kong Research Grants Council (Grant No. 16305019), and the National Natural Science Foundation of China (Grant No. 12022416).

APPENDIX A: SURFACE STATE

1. Surface state in (001)

The surface state in (001) with Sr-Pb termination is shown in Fig. 4. As we can see, there are two pairs of nontrivial surface states along $\bar{G}$-$\bar{M}$. One pair connects the valence bulk region to the conduction bulk region by crossing the boundary of the Brillouin zone. The other pair directly connects the conduction bulk region in the vicinity of the gapped cone to the valence bulk region. Similar phenomena can be observed along $\bar{G}$-$\bar{X}$. Additionally, there is one pair of trivial states along $\bar{G}$-$\bar{X}$.

2. Surface state in (110)

As we can see from Fig. 5(a), four equivalent cones with a small gap at Λ are projected to two equivalent $\bar{\Lambda}$ along $\bar{G}$-$\bar{X}$. The other two gapped cones can also be observed along $\bar{G}$-$\bar{Y}$. The reflection lines along $\bar{G}$-$\bar{X}$ and $\bar{G}$-$\bar{Y}$ are related to

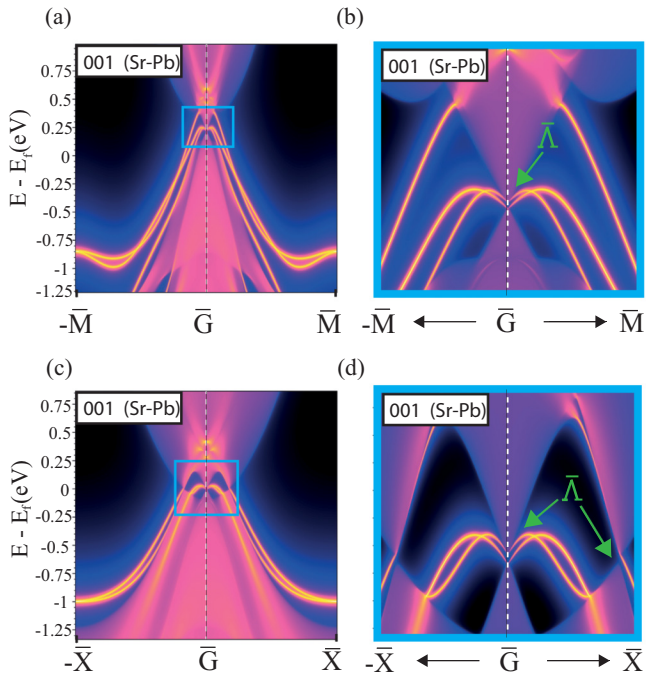

FIG. 4. (a) The surface states in (001) with Sr-Pb termination along $\bar{G}$-$\bar{M}$ direction. We zoomed in on the states near the Fermi level in (b). (c) The surface states in (001) with Sr-Pb termination along $\bar{G}$-$\bar{X}$ direction. We zoomed in on the states near the Fermi level in (d).

the reflection-invariant planes (001) and (110), respectively. Therefore, two pairs of nontrivial surface modes can be observed in Figs. 5(b) and 5(c).

3. Surface state in (111)

As shown in Fig. 5(d), two gapped cones along k_z are projected to $\bar{\Lambda}$ along the $\bar{G}$-$\bar{M}$ direction. The reflection line along $\bar{G}$-$\bar{M}$ is related to the reflection-invariant plane (110). Therefore, two pairs of nontrivial surface modes along the $\bar{G}$-$\bar{M}$ direction are clearly visible in Fig. 5(e). However, there is only one reflection line which is related to the bulk reflection plane with nonzero mirror Chern number, and we found that the surface modes along $\bar{G}$-$\bar{K}$ are gapped in Fig. 5(f).

APPENDIX B: MIRROR CHERN NUMBER

The basis of our tight-binding model is

$$\psi(k) = (\mathrm{Sr}_{1,d} \quad \mathrm{Sr}_{2,d} \quad \mathrm{Sr}_{3,d} \quad \mathrm{Pb}_{1,p}).$$

For p orbitals, the basis is $(p_z \quad p_y \quad p_x)$, and for d orbitals, the basis is $(d_{z^2} \quad d_{xz} \quad d_{yz} \quad d_{x^2-y^2} \quad d_{xy})$. We can write down how the orbitals are transformed to construct the mirror operator in real space, and then we can do the Fourier transform with the extra phase factor added. Along [100] direction, the corresponding p and d orbitals will be transformed by the following matrices:

$$R_x^p = \begin{pmatrix} 1 & 0 & 0 \\ 0 & 1 & 0 \\ 0 & 0 & -1 \end{pmatrix}, \quad R_x^d = \begin{pmatrix} 1 & 0 & 0 & 0 & 0 \\ 0 & -1 & 0 & 0 & 0 \\ 0 & 0 & 1 & 0 & 0 \\ 0 & 0 & 0 & 1 & 0 \\ 0 & 0 & 0 & 0 & 1 \end{pmatrix}. \tag{B1}$$

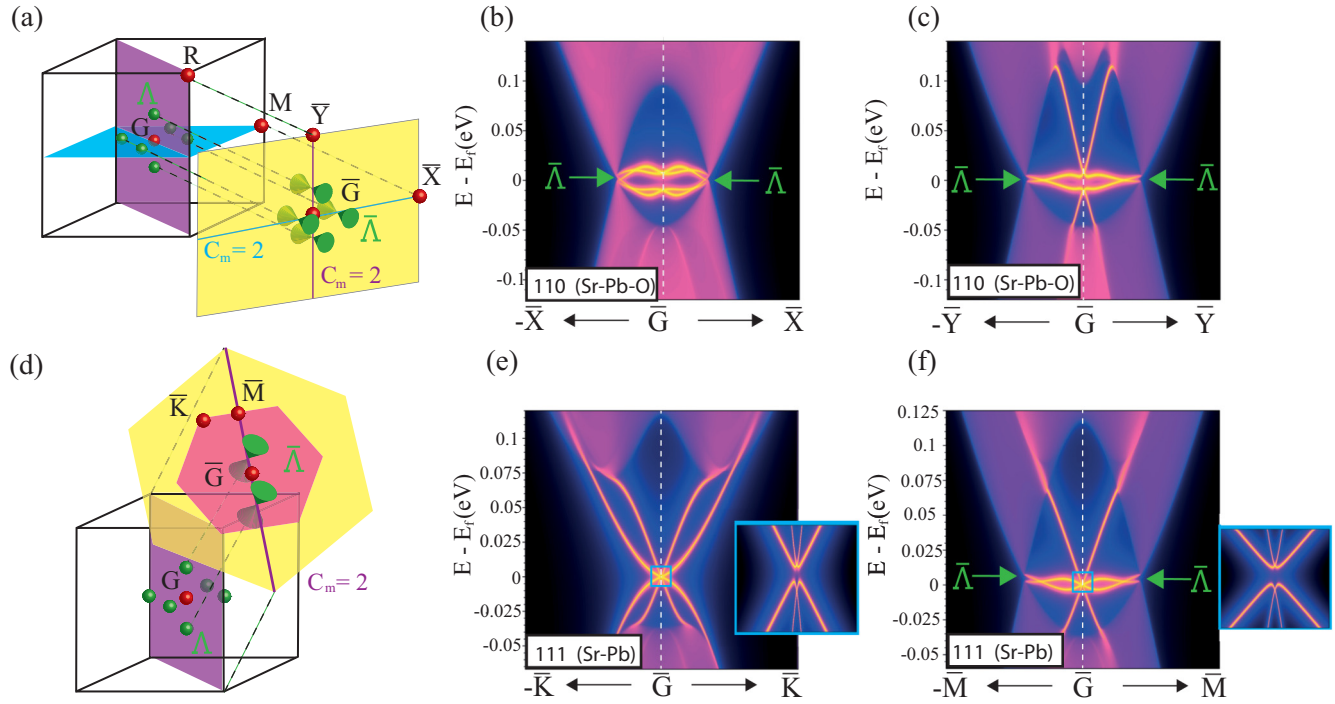

FIG. 5. (a) Projected Brillouin zone along [110] direction. [(b), (c)] The surface states in (110). (d) Projected Brillouin zone along [111] direction. [(e), (f)] The surface states in (111).

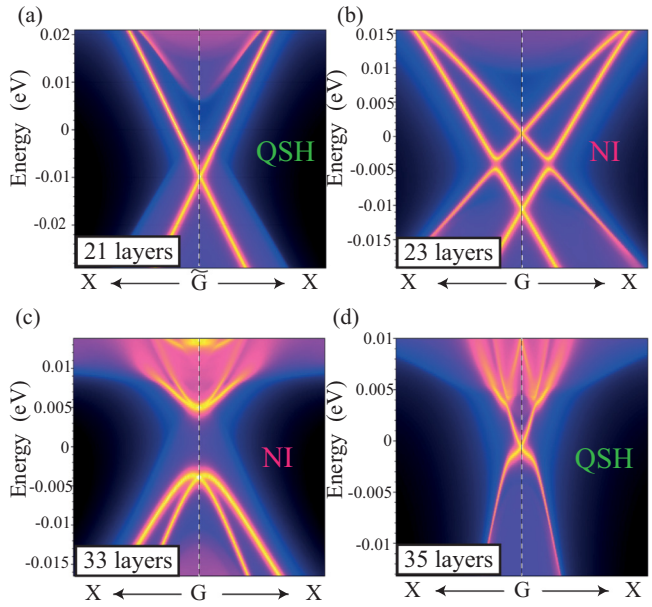

FIG. 6. The edge states of (a) 21-layer and (c) 33-layer thin films, which are QSH states. The edge states of (b) 23-layer and (d) 35-layer thin films are trivial states.

Therefore, the mirror operator in the k space is

$$R_x(k_x) = e^{i\pi\sigma_x/2} \otimes \begin{pmatrix} R_x^d & 0 & 0 & 0 \\ 0 & R_x^p e^{ik_x a} & 0 & 0 \\ 0 & 0 & R_x^p e^{ik_x a} & 0 \\ 0 & 0 & 0 & R_x^p \end{pmatrix}. \quad \text{(B2)}$$

For the [110] direction, the transformation in real space is $(x, y, z) \to (-y, -x, z)$, and the form of the operator is

$$R_{x-y}^p = \begin{pmatrix} 1 & 0 & 0 \\ 0 & 0 & -1 \\ 0 & -1 & 0 \end{pmatrix},$$

$$R_{x-y}^d = \begin{pmatrix} 1 & 0 & 0 & 0 & 0 \\ 0 & 0 & -1 & 0 & 0 \\ 0 & -1 & 0 & 0 & 0 \\ 0 & 0 & 0 & -1 & 0 \\ 0 & 0 & 0 & 0 & 1 \end{pmatrix}. \quad \text{(B3)}$$

The mirror operator along the [110] direction in the k space is

$$R_{x-y}(k_x, k_y) = e^{i\pi(\sigma_x+\sigma_y)/2\sqrt{2}} \otimes \begin{pmatrix} 0 & R_{x-y}^d e^{i(-k_x a/2 - k_y a/2)} & 0 & 0 \\ R_{x-y}^d e^{i(-k_x a/2 - k_y a/2)} & 0 & 0 & 0 \\ 0 & 0 & R_{x-y}^d e^{i(-k_x a - k_y a)} & 0 \\ 0 & 0 & 0 & R_{x-y}^p \end{pmatrix}.$$

Since the system preserves the mirror symmetry along those mirror reflection planes, the Hamiltonian must obey the commutation relation with the mirror operators along those planes. We can eventually block-diagonalize our tight-binding Hamiltonian into $\pm i$ mirror subspaces. The mirror Chern number can then be obtained by computing the Chern number on each mirror subspace.

EDGE STATE OF THIN FILM

The edge states of the thin films were calculated by the recursive Green's function method [32]. In Fig. 6, we provide the edge density of states of thin films around the critical thickness. The 21-layer thin film is a QSH state, while the 23-layer thin film is a trivial insulator. The transition from the trivial phase to the QSH phase can be observed in 33- and 35-layer thin films.

[1] C. L. Kane and E. J. Mele, Quantum spin Hall effect in graphene, Phys. Rev. Lett. **95**, 226801 (2005).

[2] B. A. Bernevig, T. L. Hughes, and S.-C. Zhang, Quantum spin Hall effect and topological phase transition in HgTe quantum wells, Science **314**, 1757 (2006).

[3] D. Hsieh, D. Qian, L. Wray, Y. Xia, Y. S. Hor, R. J. Cava, and M. Z. Hasan, A topological Dirac insulator in a quantum spin Hall phase, Nature (London) **452**, 970 (2008).

[4] Y. Xia, D. Qian, D. Hsieh, L. Wray, A. Pal, H. Lin, A. Bansil, D. Grauer, Y. S. Hor, R. J. Cava *et al.*, Observation of a large-gap topological-insulator class with a single Dirac cone on the surface, Nat. Phys. **5**, 398 (2009).

[5] L. Fu, Topological crystalline insulators, Phys. Rev. Lett. **106**, 106802 (2011).

[6] T. H. Hsieh, H. Lin, J. Liu, W. Duan, A. Bansil, and L. Fu, Topological crystalline insulators in the SnTe material class, Nat. Commun. **3**, 982 (2012).

[7] Y. Tanaka, Z. Ren, T. Sato, K. Nakayama, S. Souma, T. Takahashi, K. Segawa, and Y. Ando, Experimental realization of a topological crystalline insulator in SnTe, Nat. Phys. **8**, 800 (2012).

[8] P. Dziawa, B. Kowalski, K. Dybko, R. Buczko, A. Szczerbakow, M. Szot, E. Łusakowska, T. Balasubramanian, B. M. Wojek, M. Berntsen *et al.*, Topological crystalline insulator states in $Pb_{1-x}Sn_xSe$, Nat. Mater. **11**, 1023 (2012).

[9] S.-Y. Xu, C. Liu, N. Alidoust, M. Neupane, D. Qian, I. Belopolski, J. Denlinger, Y. Wang, H. Lin, L. A. Wray *et al.*, Observation of a topological crystalline insulator phase and topological phase transition in $Pb_{1-x}Sn_xTe$, Nat. Commun. **3**, 1192 (2012).

[10] Z. Wang, Y. Sun, X.-Q. Chen, C. Franchini, G. Xu, H. Weng, X. Dai, and Z. Fang, Dirac semimetal and topological phase transitions in A_3Bi (A = Na, K, Rb), Phys. Rev. B **85**, 195320 (2012).

[11] H. Weng, C. Fang, Z. Fang, B. A. Bernevig, and X. Dai, Weyl semimetal phase in noncentrosymmetric transition-metal monophosphides, Phys. Rev. X **5**, 011029 (2015).

[12] X. Wan, A. M. Turner, A. Vishwanath, and S. Y. Savrasov, Topological semimetal and Fermi-arc surface states in the electronic structure of pyrochlore iridates, Phys. Rev. B **83**, 205101 (2011).

[13] Z. Wang, H. Weng, Q. Wu, X. Dai, and Z. Fang, Three-dimensional Dirac semimetal and quantum transport in Cd_3As_2, Phys. Rev. B **88**, 125427 (2013).

[14] J. Liu, H. Wang, C. Fang, L. Fu, and X. Qian, van der Waals stacking-induced topological phase transition in layered ternary transition metal chalcogenides, Nano Lett. **17**, 467 (2017).

[15] C. Lei, S. Chen, and A. H. MacDonald, Magnetized topological insulator multilayers, Proc. Natl. Acad. Sci. USA **117**, 27224 (2020).

[16] A. Widera and H. Schäfer, Íbergangsformen zwischen zintl-phasen und echten salzen: Die verbindungen A_3BO (A = Ca, Sr, Ba und B = Sn, Pb), Mater. Res. Bull. **15**, 1805 (1980).

[17] T. He, Q. Huang, A. Ramirez, Y. Wang, K. Regan, N. Rogado, M. Hayward, M. Haas, J. Slusky, K. Inumara, H. Zandbergen, N. Ong, and R. Cava, Superconductivity in the non-oxide perovskite $MgCNi_3$, Nature (London) **411**, 54 (2001).

[18] M. Oudah, A. Ikeda, S. Yonezawa, T. Fukumoto, S. Kobayashi, M. Sato, and Y. Maeno, Superconductivity in the antiperovskite Dirac-metal oxide Sr_3SnO, Nat. Commun. **7**, 13617 (2016).

[19] S. Suetsugu, K. Hayama, A. W. Rost, J. Nuss, C. Mühle, J. Kim, K. Kitagawa, and H. Takagi, Magnetotransport in Sr_3PbO antiperovskite, Phys. Rev. B **98**, 115203 (2018).

[20] P. Tong, B.-S. Wang, and Y.-P. Sun, Mn-based antiperovskite functional materials: Review of research, Chin. Phys. B **22**, 067501 (2013).

[21] Y. Zhao and L. Daemen, Superionic conductivity in lithium-rich anti-perovskites, J. Am. Chem. Soc. **134**, 15042 (2012).

[22] J. Zheng, B. Perry, and Y. Wu, Antiperovskite superionic conductors: A critical review, ACS Mater. Au **1**, 92 (2021).

[23] T. H. Hsieh, J. Liu, and L. Fu, Topological crystalline insulators and Dirac octets in antiperovskites, Phys. Rev. B **90**, 081112(R) (2014).

[24] H. Nakamura and H. Takagi, Molecular beam epitaxy of three-dimensional Dirac material Sr_3PbO, APL Mater. **4**, 076101 (2016).

[25] C.-X. Liu, H. Zhang, B. Yan, X.-L. Qi, T. Frauenheim, X. Dai, Z. Fang, and S.-C. Zhang, Oscillatory crossover from two-dimensional to three-dimensional topological insulators, Phys. Rev. B **81**, 041307(R) (2010).

[26] G. Kresse and J. Hafner, *Ab initio* molecular dynamics for open-shell transition metals, Phys. Rev. B **48**, 13115 (1993).

[27] P. E. Blöchl, Projector augmented-wave method, Phys. Rev. B **50**, 17953 (1994).

[28] A. V. Krukau, O. A. Vydrov, A. F. Izmaylov, and G. E. Scuseria, Influence of the exchange screening parameter on the performance of screened hybrid functionals, J. Chem. Phys. **125**, 224106 (2006).

[29] J. P. Perdew, K. Burke, and M. Ernzerhof, Generalized gradient approximation made simple, Phys. Rev. Lett. **77**, 3865 (1996).

[30] G. Pizzi, V. Vitale, R. Arita, S. Blügel, F. Freimuth, G. Géranton, M. Gibertini, D. Gresch, C. Johnson, T. Koretsune *et al.*, Wannier90 as a community code: New features and applications, J. Phys.: Condens. Matter **32**, 165902 (2020).

[31] T. Kariyado and M. Ogata, Low-energy effective Hamiltonian and the surface states of Ca_3PbO, J. Phys. Soc. Jpn. **81**, 064701 (2012).

[32] M. P. L. Sancho, J. M. Lopez Sancho, J. M. L. Sancho, and J. Rubio, Highly convergent schemes for the calculation of bulk and surface green functions, J. Phys. F: Met. Phys. **15**, 851 (1985).

[33] T. Fukui, Y. Hatsugai, and H. Suzuki, Chern numbers in discretized Brillouin zone: Efficient method of computing (spin) Hall conductances, J. Phys. Soc. Jpn. **74**, 1674 (2005).

[34] Y. Gong, K. Zhu, Z. Li, Y. Zang, X. Feng, D. Zhang, C. Song, L. Wang, W. Li, X. Chen *et al.*, Experimental evidence of the thickness- and electric-field-dependent topological phase transitions in topological crystalline insulator SnTe (111) thin films, Nano Res. **11**, 6045 (2018).

[35] Y. Koyama, I. Tanaka, H. Adachi, Y. Uchimoto, and M. Wakihara, First principles calculations of formation energies and electronic structures of defects in oxygen-deficient $LiMn_2O_4$, J. Electrochem. Soc. **150**, A63 (2003).

[36] J. Moon, S. Kwon, M. Alahbakhshi, Y. Lee, K. Cho, A. Zakhidov, M. Kim, and Q. Gu, Surface energy-driven preferential grain growth of metal halide perovskites: Effects of nanoimprint lithography beyond direct patterning, ACS Appl. Mater. Interfaces **13**, 5368 (2021).

[37] V. Fiorentini and M. Methfessel, Extracting convergent surface energies from slab calculations, J. Phys.: Condens. Matter **8**, 6525 (1996).

[38] J. C. Boettger, Nonconvergence of surface energies obtained from thin-film calculations, Phys. Rev. B **49**, 16798 (1994).

[39] J. Liu and L. Fu, Electrically tunable quantum spin Hall state in topological crystalline insulator thin films, Phys. Rev. B **91**, 081407(R) (2015).